How to cite: *Angew. Chem. Int. Ed.* **2025**, *64*, e202506341
doi.org/10.1002/anie.202506341

Artificial Water Channels

Butterfly-Shaped Folding Synthons for Designing Superselective and Ultrapermeable Artificial Water Channels

Jie Shen[+],* *Yongqi Zhang*[+], *Yingxue Jin, Zhao-Xi Zhou, Ying Xu, Wenju Chang, Jinyu Li, Zian Lin, and Huaqiang Zeng**

Abstract: Water transport across biological membranes is essential for life, facilitated by water channel proteins like aquaporins (AQPs). Drawing inspiration from these natural systems, artificial water channels (AWCs) have emerged as transformative tools for advancing industrial and environmental applications. Herein, we report the design and comprehensive characterization of a groundbreaking class of AWCs, derived from unprecedented butterfly-shaped aromatic folding synthons, carefully engineered to emulate the functional attributes of natural AQPs. These foldamers, with their intricate helical architectures, exhibit exceptional water transport performance. Remarkably, the highest-performing AWC achieves an ultrafast water transport rate of 2.6×10^{10} H_2O s^{-1} per channel—2.4 times the efficiency of AQP1—without the need for lipid anchors to preserve its functional orientation within phospholipid bilayers, while effectively excluding salts such as NaCl and KCl, along with protons. This work presents an ideal bio-inspired, high-performance artificial alternative to natural systems, demonstrating the remarkable potential of foldamer-based AWCs as next-generation solutions for tackling critical challenges in water purification and desalination.

Introduction

The intensifying crisis of global water scarcity represents one of the most formidable challenges confronting humanity in the 21st century, with over 2 billion individuals enduring the profound consequences of inadequate access to clean and safe water.[1,2] This intricate and multifaceted predicament not only jeopardizes the delicate ecological equilibrium vital for the sustenance of life but also destabilizes the socioeconomic frameworks underpinning countless nations. Within this context of escalating urgency, membrane purification technology has emerged as a paradigm-shifting innovation, offering a highly efficient and scalable solution for water treatment and recycling. Recent strides in this transformative field have propelled researchers to explore the intricate nuances of membrane design, where the controlled construction of uniform nanopores has been identified as a critical determinant in optimizing purification performance, enhancing molecular selectivity, and ensuring long-term operational stability.[3–7]

First identified in the early 1990s, aquaporins represent a remarkable class of membrane proteins that facilitate the rapid, highly selective transport of water molecules, while simultaneously acting as effective barriers to ions and other solutes.[8–11] Notably, AQP1 is capable of transporting water at an extraordinary rate of approximately 1.1×10^{10} H_2O s^{-1} per channel, while excluding critical ions such as Na^+, K^+, Cl^-, and even protons.[12] This unique property plays an essential role in maintaining cellular osmotic balance and preserving electrochemical gradients. Despite initial efforts to harness aquaporins for incorporation into membrane materials aimed at enhancing selectivity and water permeability,[6,13] their inherent vulnerability to extreme environmental conditions—such as elevated pressures and high salinity—coupled with their relatively high production costs, has posed significant challenges, impeding their broader implementation in industrial applications.

The development of artificial water channels, meticulously engineered to replicate, and in some cases exceed, the efficiency and selectivity of natural aquaporins, holds transformative potential for advancing a wide array of water-related applications, including purification, desalination, and other critical industrial processes.[14–18] Recent research has spurred an array of inspiring designs, ranging from carbon nanotube porins,[19–21] imidazole quartets,[22–24] pillararenes,[25–28] aquafoldamers,[29–33] porous cage architectures,[34] oligoureas,[35] macrocycles,[36–38] and hydroxy channels.[39,40] To ensure their successful deployment in real-world applications, it is paramount that the water transport properties of these AWCs are on par with the exceptional performance of AQP1.

Despite the wealth of innovative designs, only three classes of high-performance AWCs have demonstrated ultrahigh water permeability that surpasses AQP1, coupled with complete salt rejection.[32,33,37] Among them, while fluorine-containing helical foldamer[33] or macrocycles[37] face

[*] Prof. Dr. J. Shen[+], Y. Zhang[+], Y. Jin, Dr. Z.-X. Zhou, Y. Xu, Dr. W. Chang, J. Li, Prof. Dr. Z. Lin, Prof. Dr. H. Zeng
College of Chemistry, Fuzhou University, Fuzhou 350116, China
E-mail: ShenJie@fzu.edu.cn
hqzeng@fzu.edu.cn
Prof. Dr. Z. Lin, Prof. Dr. H. Zeng
State Key Laboratory of Chemistry for NBC Hazards Protection
College of Chemistry, Fuzhou University, Fuzhou 350116, China
[+] Both authors contributed equally to this work.

Additional supporting information can be found online in the Supporting Information section

significant challenges in synthetic scalability, readily accessible helically folded 4-LA requires lipid anchors (LA) at its helical termini to stabilize its orientation within phospholipid bilayers.[32] Without these LAs, its water transport efficiency drops by 75%. Furthermore, the ability of LAs to enhance the water transport rate may not be sustained in the complex environment of a water purification membrane. These varying limitations emphasize the complex task of optimizing water transport characteristics across the diverse array of AWC designs. The availability of versatile, high-performance AWCs allows for tailored optimization of water permeability and selective ion rejection across a broad range of practical applications. Additionally, their potential to enhance energy efficiency, by reducing energy demands, presents opportunities for more cost-effective and sustainable solutions.

H-bonded aromatic foldamers, known for their remarkable stability, rigidity, and diverse functional potential, have emerged as an exceptionally promising platform for the design of artificial transmembrane transporters[41] including high-performance AWCs.[32,33] These foldamers present untapped opportunities for advancing innovative solutions in water transport technologies. In this study, we introduce an innovative foldamer-based AWC system $\mathbf{P}_n$ (Figure 1a) characterized by outstanding salt and proton rejection capabilities. This novel family of AWCs is constructed from previously uncharted butterfly-shaped aromatic folding synthons, intricately linked by hydrazide bonds (Figure 1b–e). The resulting architecture features a fine cavity diameter of 6.7 Å, with one-dimensional alignment of hydrazide H-atoms and pyridone O-atoms along the channel axis (Figure 1f). In a striking departure from **4-LA** design strategy, these foldamer-based AWCs $\mathbf{P}_n$ operate without the need for lipid anchors at their helical ends to maintain proper orientation within the membrane, achieving superselective, ultrapermeable water transport at an exceptional rate of 2.6×10^{10} H_2O s^{-1} per channel—approximately 2.4 times as fast as the benchmark AQP1 channel.

From both fundamental and applied perspectives, this foldamer-based class of artificial water channels stands as the first AWC to successfully integrate a comprehensive set of desirable properties, including exceptional transport efficiency, straightforward synthesis, low production cost, high conformational robustness, and outstanding chemical stability. This achievement addresses long-standing goals in the field and marks a significant advancement in the development of artificial water channels while establishing them as highly promising candidates for fabricating next-generation separation membranes in water purification and other demanding applications.

Results and Discussion

Molecular Design and Structural Features of AWCs 1–4

In our ongoing efforts to develop alternative solutions for addressing the limitations associated with current AWC systems for transmembrane water transport, we identified a notable behavior in the short trimer $\mathbf{P_{1.5}}$ (Figure 1b). Its four acylhydrazine protons are expected to form eight H-bonds with the surrounding carbonyl oxygen and pyridine nitrogen atoms (highlighted in both red and blue, Figure 1b), thereby stabilizing a linear, planar configuration (Figure 1c) that is more stable than the butterfly-shaped structure, which maintains only four H-bonds (marked in blue, Figure 1d), by 1.92 kcal mol^{-1}, as calculated at the M06-2X/6–31G(d) level (Figure S1a).[42] Intriguingly, however, crystal structure of $\mathbf{P_{1.5}}$ shown in Figure 1d reveals the breaking of four H-bonds (marked in blue, Figure 1b), resulting in the twisting of the hydrazide linkages. This disruption enables the molecule to adopt an unprecedented butterfly-shaped configuration with a dihedral angle of 75°, causing a slight destabilization of 0.7 kcal mol^{-1} (Figure S1b). This destabilization is more than offset by the formation of four intermolecular H-bonds (Figure S1c).

Intrigued by the intricately butterfly-like architecture exhibited by $\mathbf{P_{1.5}}$, we began to speculate whether this singular folding motif might serve as a blueprint to engineer a helical structure (Figure 1d). Such a transformation could unlock uncharted realms of functionality for helical foldamers, possibly expanding their utility in unprecedented and transformative ways. With this in mind, we proceeded to construct $\mathbf{P_9}$, comprising nine **AB** type repeating units and a backbone six times that of $\mathbf{P_{1.5}}$. Structural optimization at the M06-2X/6–31G(d) level clearly demonstrates that the butterfly-shaped configuration of the folding synthon $\mathbf{P_{1.5}}$ is well preserved in $\mathbf{P_9}$ because of collective stabilization by four strong intramolecular hydrogen bonds (1.8–2.3 Å) and two intramolecular C─H···π interactions between vertically aligned repeating units (Figure S1d,f). This led to the formation of a well-defined helically folded structure with three AB units per helical turn and a significantly larger helical pitch exceeding 4.6 Å.

Building upon the foundation established by $\mathbf{P_9}$, we further designed $\mathbf{P_{17}}$, a macromolecular construct comprising 17 **AB** units, which features a cavity diameter of 6.7 Å and a total height of approximately 37 Å, including the atomic thickness of the terminal units (Figure 1f). Computational molecular modeling of $\mathbf{P_{17}}$ reveals the synergistic interplay of several structural elements, including the rotatable hydrazide bonds, intramolecular hydrogen bonds, and CH–π interactions. These interactions collectively stabilize a butterfly-like conformation along the molecular backbone, akin to that observed in $\mathbf{P_{1.5}}$. This unprecedented conformation results in the alignment of hydrazide H-atoms and pyridone O-atoms in a one-dimensional array along the inner surface of the hollow cavity (Figure 1f). Furthermore, the arrangement exposes hydrazide O-atoms on the exterior surface, which may facilitate enhanced interactions between the helical structure and the H-atoms present in the alkyl chains of phospholipids. Such an alignment could potentially promote the efficient parallel orientation of the channel molecules with respect to the hydrocarbon chains within the phospholipid membrane, suggesting a mechanism for improved membrane interaction.

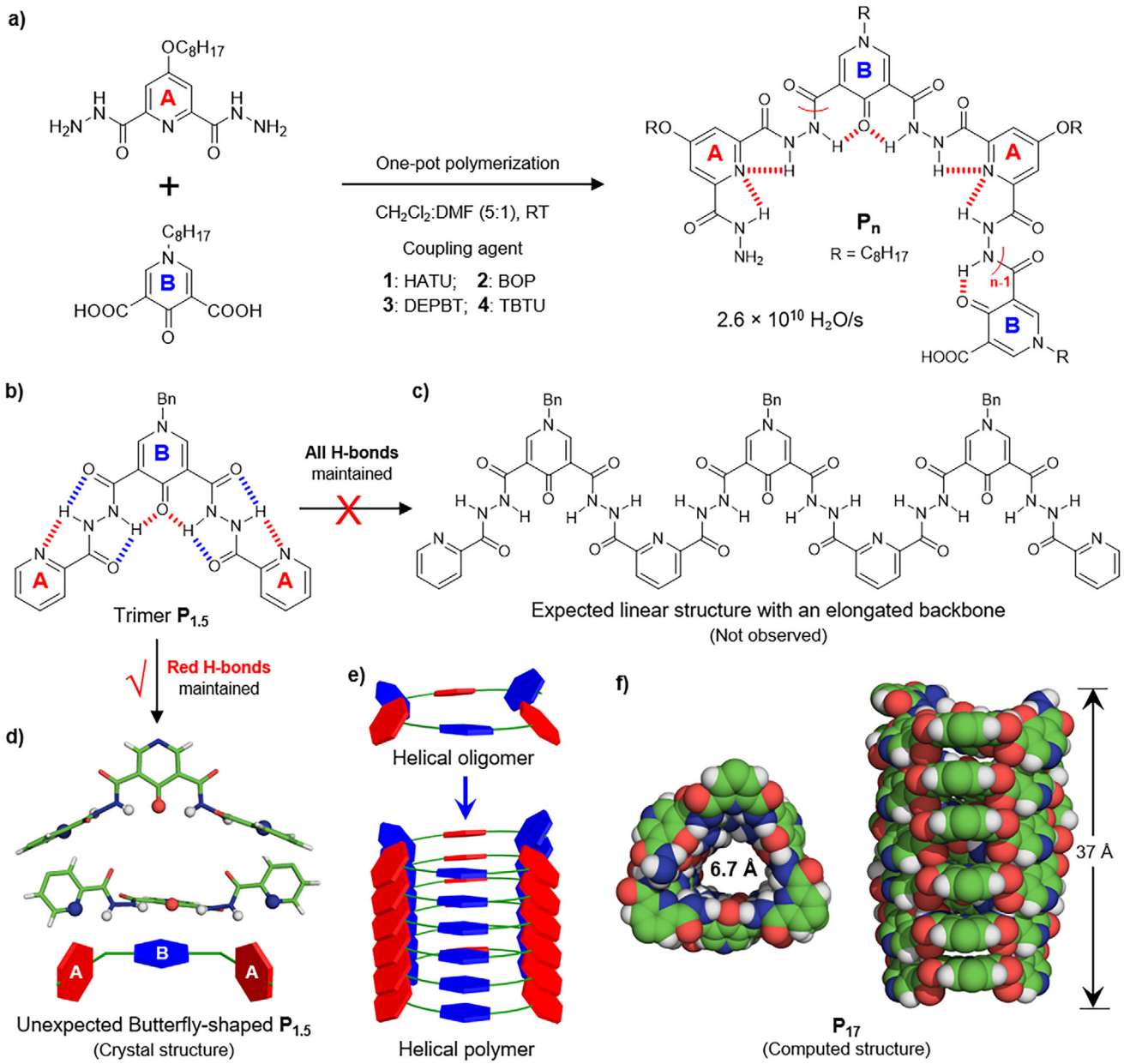

Figure 1. Molecular design and synthetic construction of aromatic foldamer based-artificial water channels built from butterfly-shaped folding synthons. a) One-pot polymerization strategies for generating foldamer-based AWCs **1**–**4**. b) Structure of trimer $\mathbf{P_{1.5}}$ made up of two **A** units and one **B** unit. c) A linear structure built on $\mathbf{P_{1.5}}$ with all H-bonds maintained, which is not observed experimentally. d) Crystal structure of $\mathbf{P_{1.5}}$ (CCDC No: 2402987), revealing a butterfly-shaped structure stabilized by four intermolecular H-bonds (Figure S1a–c). e) Schematic illustration of elongating butter-fly shaped $\mathbf{P_{1.5}}$ to build helical oligomers and membrane-spanning helical polymer channels. f) Quantum mechanics-optimized structure of $\mathbf{P_{17}}$ at the M06-2*x*/6–31G(d) level,[42] referred to as channel **2** in (b), consists of 17 **AB** units, with approximately three such units per helical turn. This configuration generates a hydrophilic lumen with a height of 3.7 nm and a diameter of 6.7 Å.

Encouraged by the promising results observed, we embarked on a systematic search for one-pot polymerization conditions (Figure 1a) that would enable the mild and efficient synthesis of membrane-spanning polymers **Pn**, exhibiting a height of approximately 3.4 nm.[43] The molecular weight (Mn) of these polymers was quantified via gel permeation chromatography (GPC). A variety of coupling reagents, including HATU, BOP, DEPBT, and TBTU, were evaluated for their ability to facilitate polymerization. Notably, BOP-mediated coupling of **A** and **B** resulted in the longest polymer, with an Mn of 9731 Da and a yield of 57% (Figure S2 and Table S1). Given the molecular weight of 582.3 Da for each **AB** repeating unit, an Mn of 9731 Da corresponds to approximately 16.7 **AB** units, and the resulting polymer was designated as **2** (or $\mathbf{P_{17}}$ shown in Figure 1f). To further corroborate these findings, an NMR-based approach was employed, wherein a chiral group was incorporated at the amine terminus to serve as an internal NMR standard (Scheme S2). By integrating the specific ^{1}H NMR signals, the molecular weight of polymer **2** was determined to be

8909 Da (Figures S3 and S4 and Table S2), a value that closely matches the GPC-derived molecular weight, thus validating the accuracy of both analytical methods.

To support the conclusions drawn from the GPC and ^{1}H NMR data, we have conducted SAXS measurements on channel **2** (e.g, $\mathbf{P_{17}}$) under both solution and solid-state conditions. Although solution-phase data exhibit significant noise, solid-state samples yield defined scattering peaks at $q = 0.24$, 0.43, and 0.71 Å^{-1}, corresponding to dimensions of 26.6, 14.6, and 8.8 Å (Figure S5d). Qualitatively, we observed three key points of agreement between the experimental and simulated SAXS patterns for $\mathbf{P_{17}}$ as inferred from Figure S5d. 1) The experimental values of 26.6 and 14.6 Å show excellent agreement with the corresponding values of 26.4 and 14.7 Å obtained from the simulated SAXS pattern (generated using ATSAS software) of the DFT-derived structure of $\mathbf{P_{17}}$. 2) Given that the simulated SAXS data for a shorter helix, such as $\mathbf{P_9}$, exhibit a smaller dimension of 23.4 Å, the slight peak flattening observed around 26.6 Å in the experimental SAXS pattern (highlighted in light blue) likely reflects the presence of helices shorter than that of $\mathbf{P_{17}}$ within the sample, which is consistent with the polymeric nature of $\mathbf{P_{17}}$. 3) By carefully comparing the fingerprint region highlighted in light red, experimental SAXS data for **2** aligns more closely with the simulated $\mathbf{P_{17}}$ than both $\mathbf{P_9}$ and $\mathbf{P_{34}}$. We have additionally conducted TEM imaging of **2** synthesized using BOP and obtained an average dimension of 3.1 ± 0.6 nm (Figure S6a,b), which is in agreement with theoretical prediction of a height of 3.7 nm and width of 2.4 nm with side chains excluded or 4.4 nm with side chains included (Figure S6c).

High Water Permeability of AWC 2

The internal cavity size of **2** measures 6.7 Å, which is significantly larger than that of a water molecule (2.5 Å) but smaller than the spatial volume by a Na^+ or K^+ ion along with its first hydration shell [of 7.5 – 10.1 Å for $[Na(H_2O)_6]^+$ and 9.0–9.6 Å for $[K(H_2O)_6]^+$ including the full van der Waals (vdW) shell (Figure S15)].[44] This size discrepancy suggests that while the cavity is sufficiently spacious to accommodate small molecules, it is too constrained to comfortably house hydrated cations. Further, the internal cavity of **2**, comprising a network of H-bond donors (acylhydrazine H-atoms) and H-bond acceptors (pyridine N-atoms and pyridone O-atoms), is endowed with a high H-bonding capacity. This unique chemical microenvironment, in combination with the cavity's size, suggests that **2** may be capable of selectively facilitating the transmembrane transport of water molecules, while potentially excluding ions due to the cavity's steric constraints and hydrophobicity. To evaluate this hypothesis, single-channel water permeability (P_{sc} in cm^3 s^{-1}) was investigated using a stopped-flow method, [16,23,31] with 0.3 M sucrose serving as the draw solution (Figure 2a). The lipid-to-channel molar ratio (mLCR) was fixed at 6000:1, and the actual channel insertion efficiencies for AWCs **1**–**4** were corrected to 70, 64, 68, and 68%, respectively. (Table S3). The resulting water permeabilities were determined to be $(12.5 \pm 0.4) \times 10^{-14}$, $(50.0 \pm 3.4) \times 10^{-14}$, $(12.7 \pm 0.9) \times 10^{-14}$, and $(19.1 \pm 1.3) \times 10^{-14}$ cm^3 s^{-1} (Figure 2b). By varying the mLCR value from 4000:1 to 10 000:1, channel **2** achieves maximum permeability at an mLCR of 8000:1, with P_{sc} value of $(58.7 \pm 1.7) \times 10^{-14}$ cm^3 s^{-1} (Figure 2c). This corresponds to a water transport rate of approximately $(2.6 \pm 0.1) \times 10^{10}$ H_2O s^{-1} per channel, representing a 1.4-fold enhancement compared to AQP1. It is worth noting that the highest permeation occurred at a specific lipid-to-channel molar ratio of 8000:1. This phenomenon results from the combined effects of variations in membrane insertion efficiency, vesicle size, blank vesicle permeability, tighter packing of channel-containing vesicles, and channel orientation (see Supporting Information for detailed analysis). In our earlier studies, such a peak was also observed at varying molar ratios, ranging from 4200:1 up to 12 000:1.[30–33,45] In addition, we have also provided the raw water permeability values (P_f, cm s^{-1}) for the channel-containing vesicles across the different lipid-to-channel ratios before normalization by channel number (Table S4).

After subtracting the DOPC background, the activation energy (Ea) for water transport through **2** was determined to be 11.95 ± 0.33 kcal mol^{-1} (Figure S11). Consistent with reported values in the literature,[14,46] the activation energy (Ea) for **2** is lower than that observed for pure lipids, indicating a reduced energy barrier for water transport. However, it remains significantly higher than the Ea value for the less permeable AQP1 (~5 kcal mol^{-1}). The faster water transport observed for **2** at the higher activation energy than AQP1 can be attributed to two primary factors. First, the larger pore diameter of 6.7 Å in **2**, compared to the more restrictive 2.8 Å diameter of AQP1, allows for a greater throughput of water molecules. Second, the multiwater configuration within the cavity of **2** contrasts with the single-file water transport that is characteristic of AQP1, reducing the overall resistance to water flow and contributing to the increased water permeability observed in **2**.[12]

High Salt Rejection by 2

A critical feature of an ideal AWC is its ability to effectively reject salts, particularly NaCl, KCl, and even protons. The salt rejection capability was initially assessed by measuring its osmotic water permeability (P_f in μm s^{-1}) under three hypertonic buffer solutions: 300 mM sucrose, 150 mM NaCl, and 150 mM KCl. With a mLCR of 8000:1, the P_f values for **2** were found to be 305.3 ± 5.4, 310.6 ± 9.4, and 309.2 ± 12.2 μm s^{-1} for sucrose, NaCl, and KCl, respectively. The corresponding reflection coefficients—defined as the ratio of P_f values—were 1.02 ± 0.01 for NaCl/sucrose and 1.01 ± 0.03 for KCl/sucrose, demonstrating that **2** achieves near-complete rejection of both NaCl and KCl. For comparison, the low reflection coefficients of 0.53 ± 0.02 for NaCl/sucrose and 0.07 ± 0.001 for KCl/sucrose,[31] obtained using gramicidin A (gA), a well-known highly permeable cation channel, further underscore the exceptional salt rejection capacity of **2**. These results confirm that **2** not only allows for efficient water transport but also effectively excludes the passage of salts, positioning it as a high performance AWC (Figure 2d).

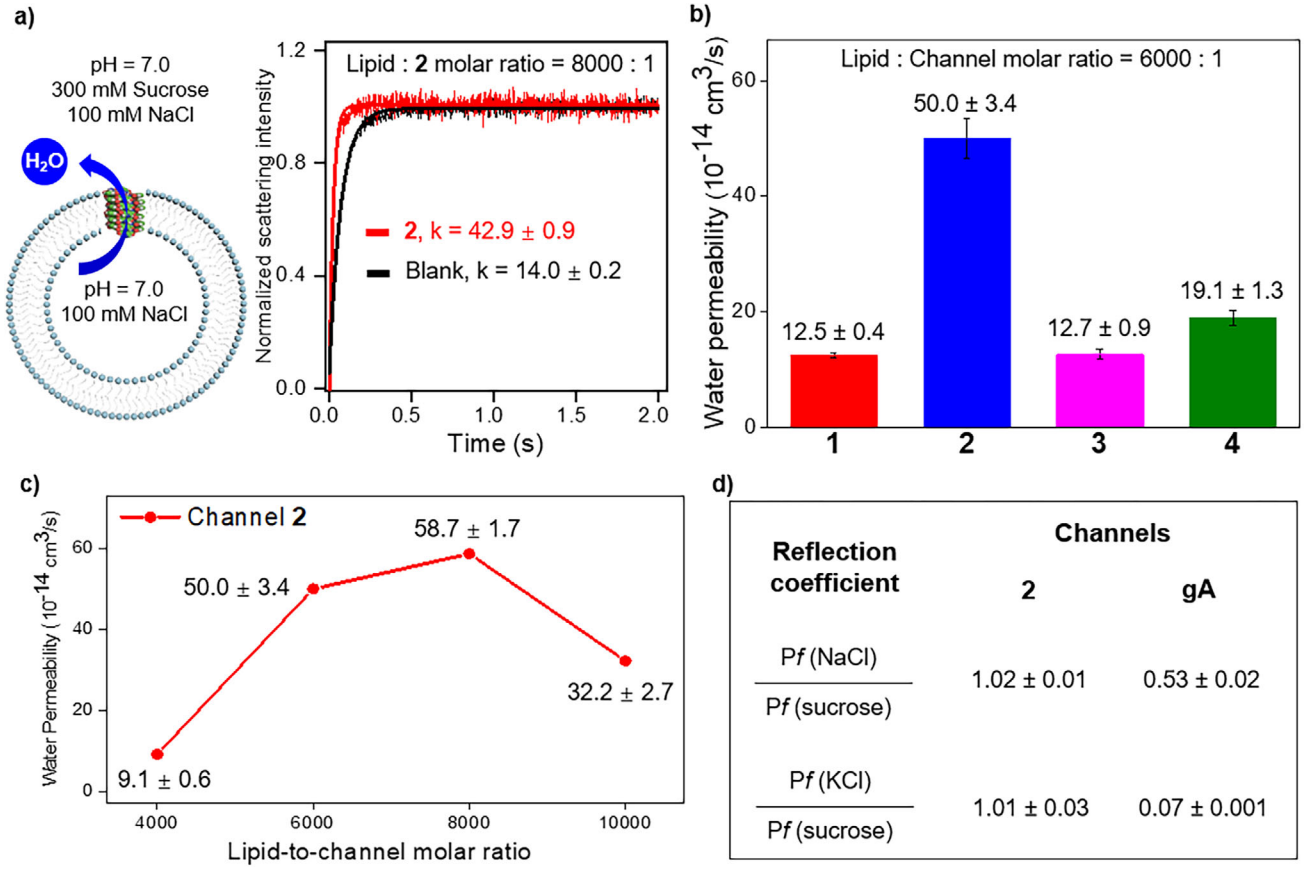

Figure 2. Ultrafast water permeation through AWCs **1**–**4**. a) Schematic illustration of LUV-based water permeability experiment, applying 300 mM sucrose to generate an inwardly directed osmotic gradient for obtaining stopped-flow light scattering traces of blank DOPC-based LUV and AWC **2**-reconstituted LUVs. b) Single-channel water permeability of AWCs **1**–**4**. c) Water permeability measurement for **2** at different lipid:channel molar ratios. d) Comparative water permeability under three different hypertonic conditions (300 mM sucrose, 150 mM NaCl and 150 mM KCl), suggesting complete and incomplete salt rejections by **2** and gramicidin A, respectively. All data represent mean ± SD from three independent experiments ($n = 3$).

The rejection of Na^+ and K^+ cations was further validated using fluorescence-based assays that incorporated pH-sensitive HPTS dyes. In this setup, the intravesicular pH was maintained at 7, while the extravesicular environment was adjusted to the same pH, but with the addition of 200 mM M_2SO_4 (where M = Na or K). Under these conditions, a high salt gradient drives H^+/M^+ antiport, which results in an increase in the pH of the intravesicular region, thereby enhancing the fluorescence intensity of HPTS. At 1 μM, **2** showed no responsiveness to either Na^+ or K^+ gradients, indicating a lack of cation transport activity. In contrast, gA at 0.1 μM was able to efficiently transport both Na^+ (110%) and K^+ (112%) cations (Figure 3a), as evidenced by significant increases in fluorescence intensity. These results are in perfect alignment with the previously determined reflection coefficients, further confirming that **2** effectively rejects cations and does not facilitate their transport, reinforcing its selective water permeability without accompanying cation passage.

The anion transport capability of water channel **2** was assessed using Cl^--sensitive SPQ dyes encapsulated in LUVs (Figue 3b). As anticipated, **2** at 1 μM shows minimal quenching of SPQ dye, with a reduction comparable to the background level (10%), indicating negligible Cl^- transport. In contrast, the well-documented Cl^- transporter **L8**,[47] at the same concentration, exhibits a significant decrease (41%) in SPQ fluorescence intensity, reflecting substantial Cl^- transport activity. These results further corroborate the selective nature of **2**, demonstrating its ability to reject not only cations but also anions like Cl^-.

High Proton Exclusion by 2

To investigate proton translocation, a pH gradient was established across the membrane (Figure 3c). Specifically, the intra-LUV contained 100 mM NaCl at pH 7, with the extravesicular region adjusted to pH 8 with 100 mM MCl (M = Li, Na, K, Rb, or Cs). If **2** were capable of proton transport, the resulting proton efflux (accompanied by the passive diffusion of Cl^- anions to maintain charge neutrality) would cause a notable increase in the intravesicular pH, thereby enhancing the fluorescence intensity of the encapsulated HPTS dye. However, experimental results reveal no significant change in fluorescence intensity upon the addition of **2** at 1 μM, indicating negligible proton transport. To quantitatively assess this, we applied a conservative methodology ("Estimation of

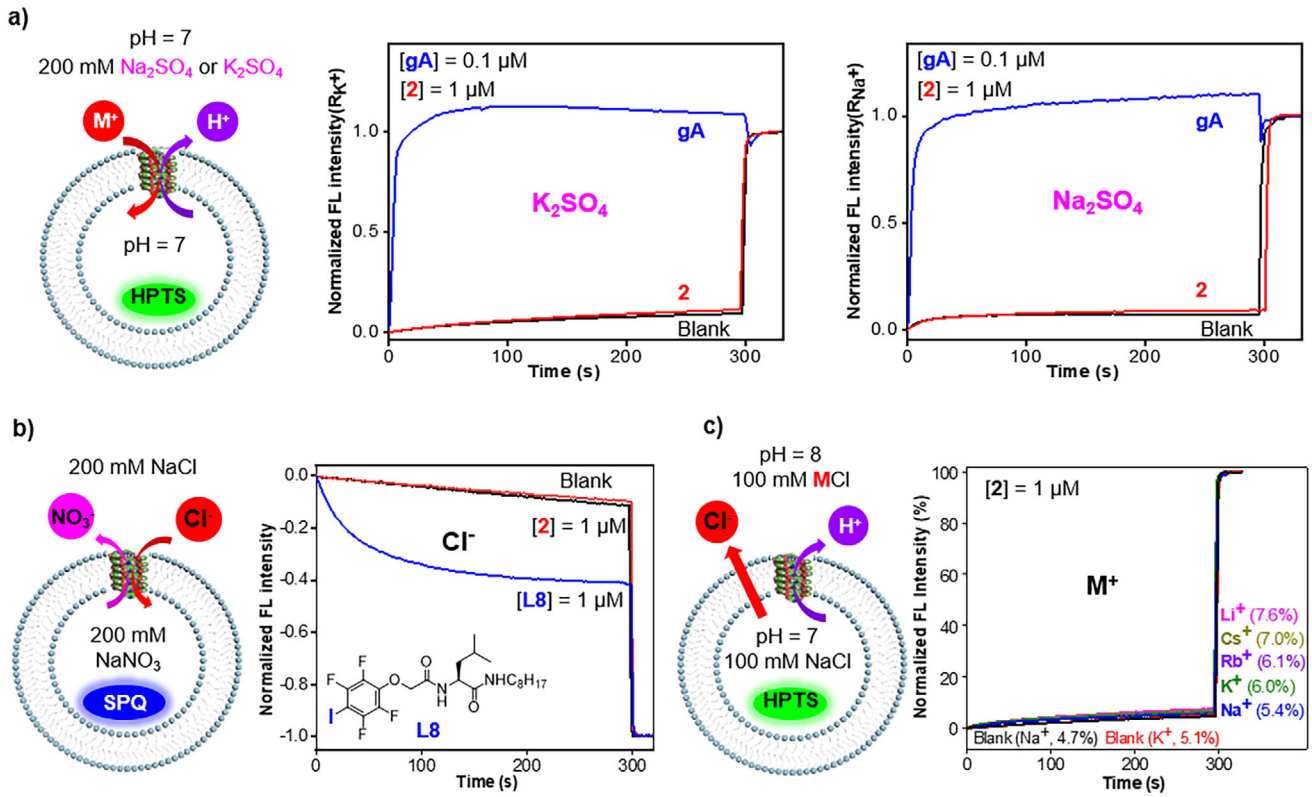

Figure 3. Salts rejection of **2**. a) HPTS-based LUV assays under high ionic concentration gradients, confirming that **2** doesn't transport Na^+ or K^+ ions. b) Chloride-sensitive SPQ assay, demonstrating that **2** does not transport anions. c) HPTS-based LUV assays under a proton gradient, establishing the inability of **2** to transport protons. HPTS = 8-hydroxypyrene-1,3,6-trisulfonic acid; SPQ = 6-Methoxy-N-(3-Sulfopropyl) Quinolinium.

Proton Transport Rate," Figure S12 for further details), which yielded an estimated proton transport rate for **2** of less than 1×10^{-2} protons s^{-1}. This corresponds to a water-to-proton selectivity ratio of approximately 2.6×10^{12}, highlighting the extreme selectivity of **2** for water transport over protons.

Computed Water Transport Rate and Selectivity for 2

As summarized in Figure 4a, **2** exhibits water permeability (2.6×10^{10} H_2O s^{-1} per channel) comparable to **4-LA** (2.7×10^{10} H_2O s^{-1} per channel)[32] and nCNTPs (2.3×10^{10} H_2O s^{-1} per channel),[20] representing a 2.4-fold enhancement over AQP1 (1.1×10^{10} H_2O s^{-1} per channel).[12] While classical nCNTPs achieve high water flux through their hydrophobic graphitic walls, **2** demonstrates remarkably high permeability despite its relatively hydrophilic lumen. This phenomenon may be attributed to the different water molecular arrangements within the channels: the ~4 Å diameter of nCNTPs restricts water molecules to single-file transport, whereas a larger 6.7 Å lumen in **2** accommodates and thus may transport multiple water molecules simutaneously. To gain further insights into the water permeability and selectivity mediated by **2** relative to AQP1, we conducted atomistic molecular dynamics (MD) simulations over a 500 ns trajectory in different salt environments.[48,49] RMSD values of all simulated systems achieved convergence (~ 0.4 nm) after approximately 50 ns. Throughout the subsequent simulation period, **2** maintained stable equilibrium conformations within the POPC membrane under both 0.6 M NaCl and 0.6 M KCl conditions (Figures 4b and S13).In the NaCl system, the simulation setup included 9312 water molecules and 78 NaCl molecules. Over the 500 ns period, AQP1 exhibits a water transport rate of 3.3×10^9 H_2O s^{-1} per channel. In contrast, **2** successfully facilitates the transport of 15 860 water molecules, corresponding to a flux of 3.17×10^{10} H_2O s^{-1} per channel (Figure 4c and Supplementary Movies 1–2). Additionally, 62 050 water molecules entered at least 1/16 of the channel length (~2.3 Å), with no Na^+ or Cl^- ions detected to traverse the channel at any point. Based on these data, the estimated water-to-NaCl selectivity ratio is at least 520, calculated as 62 050/(9312/78).

In KCl system, the water permeabilities of AQP1 and **2** were 3.3×10^9 and 3.16×10^{10} H_2O s^{-1} per channel, respectively (Figure S14a and Supplementary Movies 3–4), with the estimated water/KCl selectivity of at least 590 (= 70 453/(9312/78)).

These MD simulation results indicate that the water transport efficiency of **2** is roughly ten times that of AQP1. Furthermore, the simulations highlight **2**'s exceptional selectivity for water over Na^+, K^+, and Cl^- ions, aligning closely with the experimental findings. This high selectivity and efficiency reinforce the potential of **2** as an ideal molecular system for water transport in selective environments, further validating the experimental data on its remarkable performance.

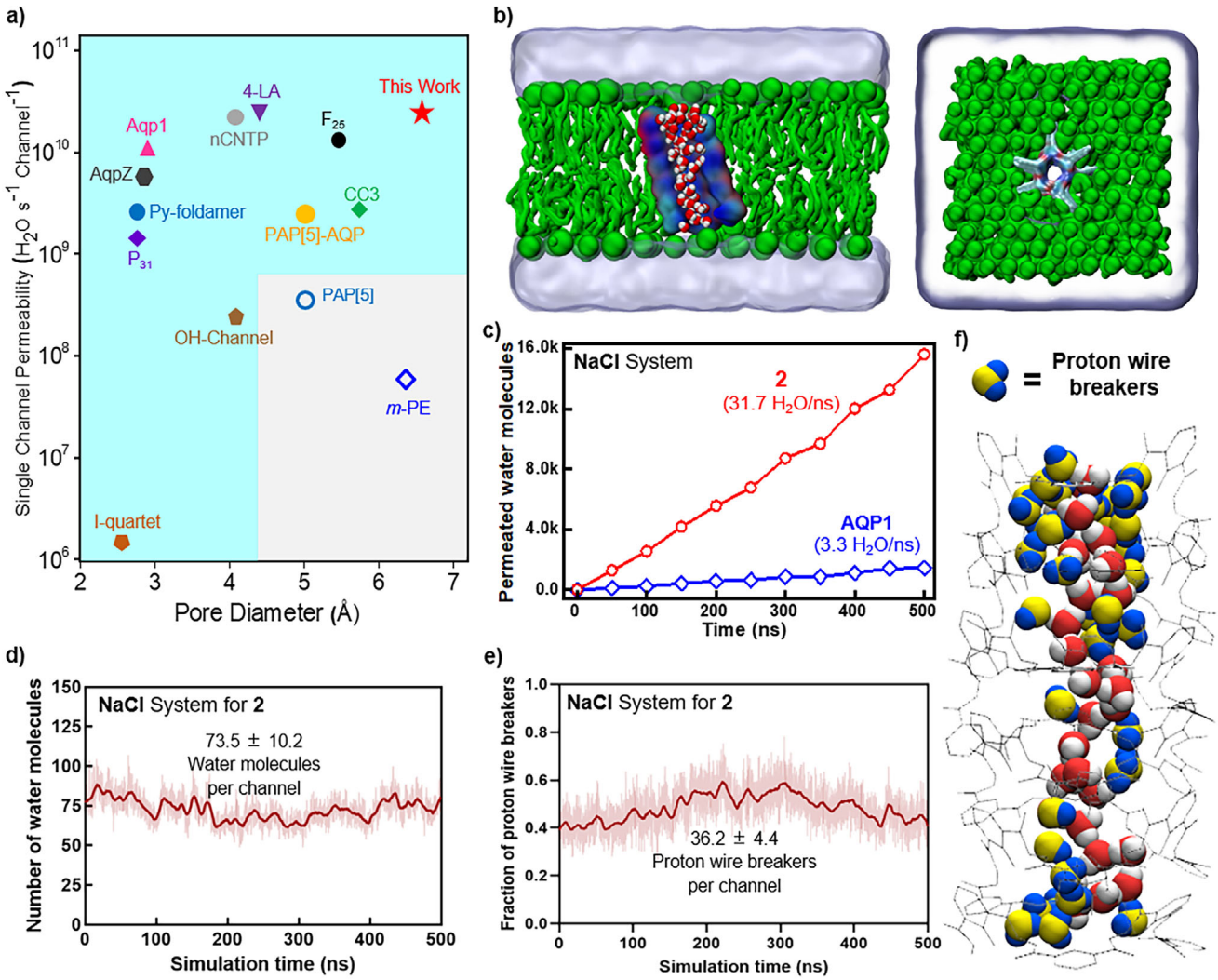

Figure 4. MD-derived water transport property of **2**. a) Single-channel water conduction rate and channel pore diameter of natural AQPs (AqpZ[10] and AQP1[12]) and AWC systems including *n*CNTP,[20] **CC3**,[34] PAP[5]-AQP,[26] **4-LA**,[32] $\mathbf{F_{25}}$,[33] Py-foldamer,[31] $\mathbf{P_{31}}$,[30] OH-channel,[39] I-quartet,[23] PAP[5][25] and m-PE[36]). Except for non-selective nCNTP, those in the light blue shaded-region exhibit salt-rejecting ability, whereas those in the grey region are ion-conductive. b) A representative snapshot of water-containing **2**, having 17 **AB** units and height of 3.7 nm, embedded in POPC membrane. c) MD-derived water transport rates for **2** and AQP1 in NaCl system. d) Number of water molecules inside the channel, with a mean of 73.5 water molecules. e) Fraction of water molecules that serve as proton wire breakers inside the channel, with a mean of 49.3% (36.2 breakers per channel). f) A water cluster consisting of 74 water molecules out of which 36 serve as proton wire breakers, preventing proton transport via the Grotthuss mechanism.

Proton Wire Breakers to Block Proton Transport through 2

Despite the presence of abundant water molecules within the lumen of **2** (Figure 4b), experimental data reveals that these water molecules do not readily facilitate proton transport. In the NaCl system, a cluster of water molecules, typically comprising 59 to 95 molecules, resides within the channel at any given moment, with an average of 73.5 water molecules occupying the lumen (Figure 4d). Among these water molecules, approximately 49.3%—or 36.2 water molecules (Figure 4e)—serve as "proton wire breakers" (Figure 4f), which interact with neighboring water molecules through zero or just one H-bond, or exclusively through two H-bonds via either O-atoms or H-atoms only (Figure 4f).[32,33] These proton wire breakers prevent the formation of a continuous H-bonded water chain across the channel, thereby inhibiting proton hopping via the Grotthuss mechanism. In the KCl system, the proportion of proton wire breakers found in **2** is slightly lower, at 47.9% (Figure S14c,d). Intriguingly, a proton breaker forming two H-bonds with adjacent water molecules exclusively through H-atoms is also observed in the NPA motif of aquaporins.[50]

Summary

In summary, the design of artificial water channels that seamlessly integrate high flux with exceptional selectivity has led to the development of a novel class of helical foldamers, constructed from unprecedented butterfly-shaped folding

synthons. The noncoplanar geometry of folding synthon creates a distinct structural advantage, significantly enhancing the contact area between the channel molecules and the alkyl chains of phospholipids. This increased interaction facilitates stable incorporation into membranes without requiring additional auxiliary groups, a feature that underscores the efficiency and elegance of the design. The size of the hydrophilic lumen with a diameter of 6.7 Å and the existence of proton wire breakers in the cavity play a pivotal role in achieving the water channel's impressive water transport rate and rejection capacity of NaCl, KCl, and protons. Intramolecular H-bonds, CH-π interaction and π–π stacking further serve to stabilize both the molecular scaffold and the lumen, reinforcing the structural integrity of the water channel while ensuring long-term stability and performance. The top-performing channel **2** stands out not only for its ultrafast water transport rate of 2.6×10^{10} H_2O s^{-1} per channel but also for its exceptional ability to reject salts and protons, achieving near-perfect selectivity. The integration of ultra-high selectivity, stability, and flux positions these helical foldamer-based water channels as a premier class of artificial water channels, offering the potential for transformative innovations across a wide range of pioneering applications in both industrial and biomedical fields. These range from advancing artificial water channel-based seawater reverse osmosis membranes to addressing diseases associated with malfunctioning natural water channels, such as certain kidney disorders or neurodegenerative diseases.

Acknowledgements

This work is supported by the National Natural Science Foundation of China (22271049 and 22371048), the "Chu Ying Program" for the Top Yong Talents of Fujian Province, Natural Science Foundation of Fujian Province (2023J01054) and a start-up grant from Fuzhou University.

Conflict of Interests

The authors declare no conflict of interest.

Data Availability Statement

The data that support the findings of this study are available from the corresponding author upon reasonable request.

Keywords: Artificial water channels · Proton rejection · Salt rejection · Supramolecular chemistry · Water desalination

[1] C. He, Z. Liu, J. Wu, X. Pan, Z. Fang, J. Li, B. A. Bryan, *Nat.Commun.* **2021**, *12*, 4667.
[2] J. Eliasson, *Nature Water.* **2024**, *2*, 298–299.
[3] A. Lee, J. W. Elam, S. B. Darling, *Environ. Sci.: Water Res. Technol.* **2016**, *2*, 17–42.
[4] P. Wagh, I. C. Escobar, *Environ. Prog. Sustainable Energy* **2019**, *38*, e13215.
[5] E. Abaie, L. Xu, Y.-x. Shen, *Front. Environ. Sci. Eng.* **2021**, *15*, 124.
[6] L. Sharma, L. Ye, C. Yong, R. Seetharaman, K. Kho, W. Surya, R. Wang, J. Torres, *J. Membr. Sci.* **2022**, *654*, 120551.
[7] H. Oh, L. Samineni, R. J. Vogler, C. Yao, H. Behera, R. Dhiman, A. Horner, M. Kumar, *ACS Nano* **2025**, *19*, 31–53.
[8] K. Murata, K. Mitsuoka, T. Hirai, T. Walz, P. Agre, J. B. Heymann, A. Engel, Y. Fujiyoshi, *Nature* **2000**, *407*, 599–605.
[9] P. Agre, *Proc Am Thorac Soc.* **2006**, *3*, 5–13.
[10] A. Horner, C. Siligan, A. Cornean, P. Pohl, *Faraday Discuss.* **2018**, *209*, 55–65.
[11] H. Tan, M. Duan, H. Xie, Y. Zhao, H. Liu, M. Yang, M. Liu, J. Yang, *Sci. Adv.* **2024**, *10*, eade9520.
[12] A. Horner, F. Zocher, J. Preiner, N. Ollinger, C. Siligan, S. A. Akimov, P. Pohl, *Sci. Adv.* **2015**, *1*, e1400083.
[13] Y. Li, Y. Zhao, H. Wang, M. Wang, *Desalination* **2019**, *468*, 114081.
[14] B. Gong, *Faraday Discuss.* **2018**, *209*, 415–427.
[15] W. Si, P. Xin, Z.-T. Li, J.-L. Hou, *Acc. Chem. Res.* **2015**, *48*, 1612–1619.
[16] Y. J. Lim, K. Goh, R. Wang, *Chem. Soc. Res.* **2022**, *51*, 4537–4582.
[17] W. Song, M. Kumar, *Langmuir* **2022**, *38*, 9085–9091.
[18] D.-D. Su, M. Barboiu, *Coord. Chem. Rev.* **2024**, *515*, 215973.
[19] R. H. Tunuguntla, F. I. Allen, K. Kim, A. Belliveau, A. Noy, *Nat. Nanotechnol.* **2016**, *11*, 639–644.
[20] R. H. Tunuguntla, R. Y. Henley, Y.-C. Yao, T. A. Pham, M. Wanunu, A. Noy, *Science* **2017**, *357*, 792–796.
[21] Y. Li, Z. Li, F. Aydin, J. Quan, X. Chen, Y.-C. Yao, C. Zhan, Y. Chen, P. Tuan Anh, A. Noy, *Sci. Adv.* **2020**, *6*, eaba9966.
[22] Y. Le Duc, M. Michau, A. Gilles, V. Gence, Y.-M. Legrand, A. Van Der Lee, S. Tingry, M. Barboiu, *Angew. Chem. Int. Ed.* **2011**, *50*, 11366–11372.
[23] E. Licsandru, I. Kocsis, Y.-x. Shen, S. Murail, Y.-M. Legrand, A. van der Lee, D. Tsai, M. Baaden, M. Kumar, M. Barboiu, *J. Am. Chem. Soc.* **2016**, *138*, 5403–5409.
[24] M. Di Vincenzo, A. Tiraferri, V.-E. Musteata, S. Chisca, R. Sougrat, L.-B. Huang, S. P. Nunes, M. Barboiu, *Nat. Nanotechnol.* **2021**, *16*, 190–196.
[25] Y.-X. Shen, W. Si, M. Erbakan, K. Decker, R. De Zorzi, P. O. Saboe, Y. J. Kang, S. Majd, P. J. Butler, T. Walz, A. Aksimentiev, J.-L.i Hou, M. Kumar, *Proc. Natl. Acad. Sci. USA* **2015**, *112*, 9810–9815.
[26] Z.-J. Yan, D. Wang, Z. Ye, T. Fan, G. Wu, L. Deng, L. Yang, B. Li, J. Liu, T. Ma, C. Dong, Z.-T. Li, L. Xiao, Y. Wang, W. Wang, J.-L. Hou, *J. Am. Chem. Soc.* **2020**, *142*, 15638–15643.
[27] I.-M. Andrei, D. Strilets, S. Fa, M. Baaden, T. Ogoshi, M. Barboiu, *Angew. Chem. Int. Ed.* **2023**, *62*, e202310812
[28] Q. Xiao, T. Fan, Y. Wang, Z.-T. Li, J.-L. Hou, Y. Wang, *CCS Chem* **2023**, *5*, 1745–1752.
[29] Y. Huo, H. Zeng, *Acc. Chem. Res.***2016**, *49*, 922–930.
[30] J. Shen, J. Fan, R. Ye, N. Li, Y. Mu, H. Zeng, *Angew. Chem. Int. Ed.* **2020**, *59*, 13328–13334.
[31] J. Shen, R. Ye, A. Romanies, A. Roy, F. Chen, C. Ren, Z. Liu, H. Zeng, *J. Am. Chem. Soc.* **2020**, *142*, 10050–10058.
[32] A. Roy, J. Shen, H. Joshi, W. Song, Y.-M. Tu, R. Chowdhury, R. Ye, N. Li, C. Ren, M. Kumar, A. Aksimentiev, H. Zeng, *Nat. Nanotechnol.* **2021**, *16*, 911–917.
[33] J. Shen, A. Roy, H. Joshi, L. Samineni, R. Ye, Y.-M. Tu, W. Song, M. Skiles, M. Kumar, A. Aksimentiev, H. Zeng, *Nano Lett.* **2022**, *22*, 4831–4838.
[34] D. Yuan, J. Dong, J. Liu, D. Zhao, H. Wu, W. Zhou, H. Gan, Y. Tong, J. Jiang, D. Zhao, *Nat. Commun.* **2020**, *11*, 4927.
[35] C. Dutta, *Chem* **2023**, *9*, 2048–2050.

[36] X. Zhou, G. Liu, K. Yamato, Y. Shen, R. Cheng, X. Wei, W. Bai, Y. Gao, H. Li, Y. Liu, F. Liu, D. M. Czajkowsky, J. Wang, M. J. Dabney, Z. Cai, J. Hu, F. V. Bright, L. He, X. C. Zeng, Z. Shao, B. Gong, *Nat. Commun.* **2012**, *3*, 949.
[37] Y. Itoh, S. Chen, R. Hirahara, T. Konda, T. Aoki, T. Ueda, I. Shimada, J. J. Cannon, C. Shao, J. Shiomi, K. V. Tabata, H. Noji, K. Sato, T. Aida, *Science* **2022**, *376*, 738–743.
[38] I. M. Andrei, A. Chaix, B. T. Benkhaled, R. Dupuis, C. Gomri, E. Petit, M. Polentarutti, A. van der Lee, M. Semsarilar, M. Barboiu, *J. Am. Chem. Soc.* **2023**, *145*, 21213–21221.
[39] L.-B. Huang, A. Hardiagon, I. Kocsis, C.-A. Jegu, M. Deleanu, A. Gilles, A. van der Lee, F. Sterpone, M. Baaden, M. Barboiu, *J. Am. Chem. Soc.* **2021**, *143*, 4224–4233.
[40] D. Mondal, B. R. Dandekar, M. Ahmad, A. Mondal, J. Mondal, P. Talukdar, *Chem. Sci.* **2022**, *13*, 9614–9623.
[41] D. Zhang, W. Chang, J. Shen, H. Zeng, *Chem. Commun.* **2024**, *60*, 13468–13491.
[42] Y. Zhao, D. G. Truhlar, *Theor. Chem. Acc.* **2008**, *120*, 215–241.
[43] T. Kobayashi, A. K. Menon, *Curr. Biol.* **2018**, *28*, R386–R391.
[44] J. Mähler, I. Persson, *Inorg. Chem.* **2012**, *51*, 425–438.
[45] G.-P. Cao, Z.-H. Yang, H. Zhao, J. Shen, W. Chang, Z. Liu, H. Zeng, *Org. Chem. Front.* **2025**, *12*, 1603–1611.
[46] B. L. De Groot, H. Grubmüller, *Science* **2001**, *294*, 2353–2357.
[47] C. Ren, X. Ding, A. Roy, J. Shen, S. Zhou, F. Chen, S. F. Yau Li, H. Ren, Y.i Y. Yang, H. Zeng, *Chem. Sci.* **2018**, *9*, 4044–4051.
[48] J. M. Wang, R. M. Wolf, J. W. Caldwell, P. A. Kollman, D. A. Case, *J. Comput. Chem.* **2004**, *25*, 1157–1174.
[49] D. Case, K. Belfon, I. Ben-Shalom, S. R. Brozell, D. Cerutti, T. Cheatham, Cruzeiro, III, T. A. Darden, R. Duke, G. Giambasu, M. Gilson, H. Gohlke, A. Götz, R. Harris, S. Izadi, S. A. Izmailov, K. Kasavajahala, A. Kovalenko, R. Krasny, P. Kollman, *Amber.* **2020**, *20*, 35–852.
[50] U. Kosinska Eriksson, G. Fischer, R. Friemann, G. Enkavi, E. Tajkhorshid, R. Neutze, *Science* **2013**, *340*, 1346–1349.

Manuscript received: March 19, 2025
Revised manuscript received: July 30, 2025
Accepted manuscript online: August 04, 2025
Version of record online: August 17, 2025